Surface & Coatings Technology 297 (2016) 51–57

Contents lists available at ScienceDirect

Surface & Coatings Technology

journal homepage: www.elsevier.com/locate/surfcoat

Electrodeposition and biomineralization of nano-β-tricalcium phosphate on graphenated carbon nanotubes

N. Metoki [a,1], C.M.R. Rosa [b,1], H. Zanin [c], F.R. Marciano [b], N. Eliaz [a], A.O. Lobo [b,*]

[a] Department of Materials Science and Engineering, Tel-Aviv University, Ramat Aviv, Tel Aviv 6997801, Israel
[b] Laboratory of Biomedical Nanotechnology (Nanobio), Institute of Research and Development, University of Vale do Paraiba, Av. Shishima Hifumi, 2911, São Jose dos Campos 12244-000, SP, Brazil
[c] Laboratory of Energy Storage & Supply (ES&S), Institute of Research and Development, University of Vale do Paraíba, Av. Shishima Hifumi, 2911, São Jose dos Campos 12244-000, SP, Brazil

ARTICLE INFO

Article history:
Received 23 February 2016
Revised 15 April 2016
Accepted in revised form 16 April 2016
Available online 20 April 2016

Keywords:
Reduced graphene oxide (rGO)
Graphenated carbon nanotube (CNT)
Calcium phosphate (CaP)
Tricalcium phosphate (TCP)
Biomineralization
Electrodeposition

ABSTRACT

Nano-calcium-phosphate (n-CaP) is an attractive, biocompatible material for increasing osteointegration. Among nanomaterials, functionalized carbon-based materials are emerging materials, which have excellent mechanical properties, biocompatibility and chemical stability. These properties may further enhance the n-CaP performance. It has been shown that stoichiometric n-CaP can be electrodeposited on graphene and carbon nanotubes (CNTs) by employing fast and low-cost electrodeposition techniques. Here, we present, for the first time, a crystalline, needle-like nano-β-tricalcium phosphate (n-β-TCP) electrodeposited on reduced graphene oxide (rGO) nanosheets. The rGO was grown on CNT, as a composite biomaterial, in a one-step process, followed by electrodeposition of n-CaP. The results show that, in acidic pH, needle-like crystals appear on the surface. It is speculated that the carboxyl (carboxylic acid)/carboxylate functional groups attached directly to the rGO are essential in accelerating OH^- formation and deposition of needle-like n-CaP crystals. High-resolution scanning electron microscopy, transmission electron microscopy, energy dispersive X-ray spectroscopy, and X-ray diffraction elucidated homogeneous, highly crystalline, n-CaP (β-tricalcium phosphate) crystals. This composite presented an excellent *in vitro* biomineralization after soaking in simulated body fluid.

1. Introduction

Calcium phosphates (CaPs) are a family of ceramics, some of which (including hydroxyapatite, HAp, octacalcium phosphate, OCP, and tricalcium phosphate, TCP) are approved for clinical use, *e.g.* for improving osteointegration of orthopedic and dental implants [1,2]. However, they suffer from poor mechanical properties in tension [3–5]. HAp is mainly used as a coating on titanium implants and is commonly applied by plasma spray [6–8].

In order to address the mechanical deficiencies and increase the bioactivity of the scaffold, sintered composites of HAp reinforced with polymers, silica or carbon-based material have been used [3,9]. For example, Mukherjee et al. showed that by addition of 1 wt.% carbon nanotube (CNT) to HAp, the composite's mechanical properties showed significant improvement in toughness (120% increase) without significant tradeoff in hardness or stiffness [10]. Baradaran et al. [11] studied the biological and mechanical performance of pure HAp *versus* reduced graphene oxide (rGO)/HAp composite. The elastic modulus and fracture toughness were compared. It was found that the values of both properties increased by 86% and 40%, respectively, while promoting osteoblasts adhesion and proliferation. Another method commonly used to synthesize HAp-carbon based composites is freeze-drying. For example, Manitha et al. [12] presented graphene oxide (GO) composite incorporated with gelatin and HAp using a freeze-drying technique. It was shown that the addition of GO to the scaffold enhanced the tensile properties. Moreover, the composite showed biodegradable properties and ability to induce osteogenic differentiation without added supplements. Xiong et al. [13] showed that the addition of 1 wt.% of GO improves the GO/HAp/sodium alginate composite's compressive strength and modulus by 23.2% and 28.3%, respectively. Wet synthesis methods have also been explored. For example, Lee et al. [14] showed a reduced GO-coated HAp composite created from suspended solution. The GO addition to the HAp was shown to enhance spontaneous osteogenic differentiation of hMSCs without hindering their proliferation.

It was demonstrated that CaP/carbon-based coatings can be made using electrophoretic deposition (EPD). For example, Li et al. showed EPD of GO-hyaluronic acid-HAp nanocomposite coating on titanium substrate [15]. The addition of GO to the coating increased the deposition rate and inhibited cracks in the coating. More recently, Li et al. [16] have also shown GO/HAp coating on commercially pure titanium using EPD. The addition of GO to the coating increased the adhesion of the coating to the substrate and reduced cracking in the coating. Santos

* Corresponding author.
E-mail addresses: aolobo@pq.cnpq.br, lobo.aol@gmail.com (A.O. Lobo).
[1] These authors contributed equally to this work.

http://dx.doi.org/10.1016/j.surfcoat.2016.04.035
0257-8972/

et al. [17] presented GO/HAp nanoparticles coating on ultrahigh-purity magnesium substrate. The coating was found to promote surface hydrophilic behavior and to decrease the coating's degradation rate.

An alternative way to create a carbon/HAp composite is by electrodeposition (ED) of HAp on carbon substrates. For example, Lobo et al. [18] developed a highly efficient, fast method of ED HAp on vertically aligned CNTs oxidized as a substrate. It was shown that thin, homogeneous film with high crystallinity can be formed without additional heat treatment. Also, Zhang et al. electrodeposited HAp on CNTs/carbon fibers hybrid materials [19]. They produced stoichiometric nanocrystals similar to the structure found in human bone. More recently, Lobo et al. have produced CNT/nHAp and polymer/CNT/nHAp composites using ED for tissue engineering [20–23]. They observed formation of a thin homogeneous film with high crystallinity without any thermal treatment and with bioactivity properties that accelerate *in vitro* biomineralization, osteoblast adhesion and *in vivo* lamellar bone formation. Siqueira et al. [20] showed *in situ* ED of nHAp on freestanding aligned CNTs porous scaffold. It was shown that the composite is biocompatible and is able to promote cell adhesion. Zanin et al. [22] showed direct ED of nHAp onto rGO at pH 4. Results showed that the carboxyl groups attached to the rGO were essential to accelerate the deposition of nHAp and the formation of crystals on the surface, as well as mesenchymal stem cells adhesion to the coating.

Yet, highly crystalline, needle-like n-CaP directly electrodeposited on rGO/CNT nanomaterials has never been demonstrated before, to the best of our knowledge. Here, we present the direct ED of nanotricalcium phosphate (n-TCP) crystals from two electrolyte solutions at two acidic pH values on porous rGO nanosheets grown on CNT. This coating is further characterized by high-resolution scanning electron microscopy (HR-SEM), high-resolution transmission electron microscopy (HR-TEM), energy-dispersive X-ray spectroscopy (EDS), and X-ray diffraction (XRD). In addition, the bioactivity of the new composite is evaluated *in vitro* by immersion in simulated body fluid (SBF).

2. Experimental

2.1. One-step synthesis of rGO nanosheets grown on CNT

Graphenated CNTs were grown on titanium substrates, 10 mm × 10 mm × 1 mm in size, as described earlier by Zanin et al. [24]. The substrates were pretreated using a two-step process: 1) immersion in polyaniline solution, and 2) immersion in a nickel nitrate solution. The substrate was immersed in each solution for 2 h at room temperature and subsequently dried. Next, a hot filament chemical vapor deposition (HFCVD) was employed. A mixture of propanone:camphor:citric acid (1:1:1 by volume) was used as a carbon source; it was dragged to the deposition chamber by hydrogen gas (15 cm^2/min). The chamber was maintained at 10 Torr with a flux of 65 cm^2/min and 20 cm^2/min of nitrogen and oxygen gases, respectively. Vapor deposition was done for 30 min at 1500 °C using a spiral tungsten filament, forming a microporous rGO nanosheet on CNTs.

2.2. Electrodeposition of n-CaP crystals on porous rGO films

The ED of the n-CaP crystals onto the porous rGO films was performed using 0.042 M $Ca(NO_3)_2 \cdot 4H_2O$ and 0.025 M $(NH_4)_2HPO_4$ electrolytes at pH 5.8 and 3.8, as described in [22]. Briefly, the electrochemical experiment was carried out using a three-electrode cell coupled to an Autolab PGSTAT 128 N potentiostat/galvanostat equipped with pH and temperature module control (pX1000). Porous rGO films were employed as the working electrode. The area in contact with the electrolyte solution was 0.062 cm^2. A high-purity platinum wire served as an auxiliary electrode, and an Ag/AgCl (3 M KCl) electrode was used as the reference electrode. The n-CaP films were produced by applying a constant potential of −2.0 V for 30 min. The solution temperature was maintained at 74.5 ± 0.5 °C. This value was chosen by trial and error.

2.3. Characterization of rGO/n-CaP

Field–emission gun SEMs, models JEOL 6330 and FEI Inspect F50, and SEM model Zeiss EVO Ma10 coupled with Inca Penta FET ×3 EDS system from Oxford Instruments were used to characterize the surface morphology of both porous rGO and rGO/n-CaP. Micrographs were taken before and after the biomineralization assay. HR-SEM (FEI Magellan 400 L) and XRD (Philips X-Pert) with Cu-Kα radiation generated at 40 kV and 50 mA were used to characterize the microstructure and phase content of the n-CaP crystals. The experimental spectra were compared to the JCPDS standards for HAp ($Ca_5(PO_4)_3(OH)$, 09-0432), OCP ($Ca_4(HPO_4)(PO_4)_2 \cdot 2.5H_2O$, 44-0778 and 26-1056), α-TCP (α-$Ca_3(PO_4)_2$, 09-0348 and 29-0359), β-TCP (whitlockite, β-$Ca_3(PO_4)_2$, 09-0169), brushite (dibasic calcium phosphate dehydrate, DCPD or $CaHPO_4 \cdot 2H_2O$, 09-0077 and 11-0293), monetite (dibasic calcium phosphate anhydrous, DCPA or $CaHPO_4$, 09-0080, 04-0513 and 03-0398), and titanium (44-1294). EDS analysis was used to determine semi-quantitatively the content of calcium (Ca) and phosphorus (P).

2.4. Biomineralization assay

An aqueous solution, five times more concentrated than that found in the human blood plasma, was prepared from high chemical grade reagents (Sigma-Aldrich), see Table 1. The pH of the solution was measured by a pH meter (Metrohm) and adjusted to 7.40 ± 0.35 (by adding NaOH), to match that of the blood plasma.

Biomineralization was evaluated on the rGO/n-CaP composite by immersing the substrate in 15 mL polyethylene vials containing SBF, up to 21 days. The vials were kept in a refrigerated benchtop incubator (Cientec CT-713), shaken at 75 rpm at a temperature of 36.5 ± 0.1 °C. The pH values were monitored using a pH meter throughout the experiment. After incubation time, the samples were washed with deionized water at ~65 °C. The samples were characterized after 14 and 21 days of immersion using FEG-SEM. XRD analysis was performed on the samples after 21 days.

2.5. Thermodynamic predictions of precipitation of CaPs from solution

A geochemical computer program (PHREEQC) was used to calculate, based on thermodynamic principles, the saturation indices (SIs, namely, the tendency to precipitate from solution) of the different CaP phases as a function of pH [6].

3. Results and discussion

Fig. 1(a, b, c) presents morphological details of as-grown graphenated CNTs material. It can be seen in Fig. 1(a), a top view of graphene film, that the sample has a porous morphology consisted of entangled tubes. The diameter of the tubes varies from 60 nm to 1 μm (Fig. 1(b) and (c)). The average diameter of the CNTs is 450 nm ± 30 nm. A higher magnification image, Fig. 1(b), reveals

Table 1
Chemical composition of SBF × 5 solution.

Chemical	Concentration [mM]
NaCl	92.88
KCl	2.60
K_2HPO_4	2.03
$CaCl_2 \cdot 2H_2O$	4.27
$MgCl_2 \cdot 6H_2O$	3.54
$NaHCO_3$	4.10
Na_2SO_4	0.83

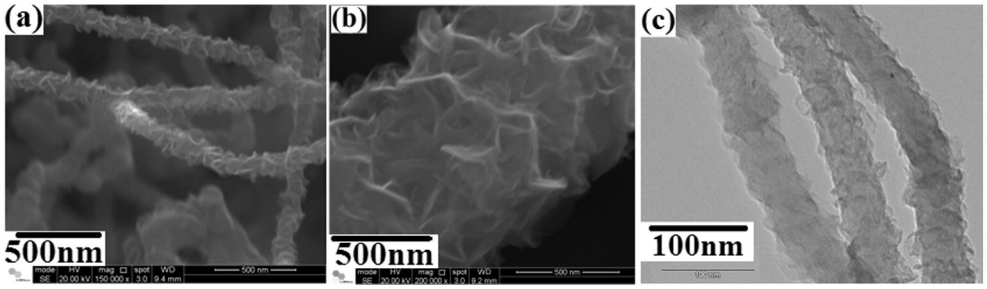

Fig. 1. Typical SEM (a, b) and TEM (c) micrographs of as-grown micro-porous rGO.

graphene nanosheets along the outer CNT surfaces. CNTs are decorated with graphene nanosheets growing radial to the tube axis, which had probably built-up of residual strain followed by buckling to nucleate a graphitic-edge protrusion from the CNTs' sidewall [24]. Fig. 1(c) presents TEM micrograph based on which the graphene interplanar spacing is 0.35 nm and graphene sheet length is 20 nm.

EDS spectra were acquired to identify the chemical composition of as-grown micro-porous rGO. The sample was found to be composed mainly of carbon and oxygen. Impurities such as Si, Ni and Fe were found at trace levels; they are attributed to the substrate's synthesis. Titanium was not detected in the EDS spectra, indicating that the carbon layer is at least 3 μm thick. The oxygen found in the sample was introduced during the rGO growth, while preparing the film. It attaches to the carbon nanosheets and tube surfaces as oxygen-containing functional groups [22]. These functional groups can be highly beneficial for enhanced growth of HAp, as reported before by Zanin et al. [23]. The atomic hydrogen introduced to the chamber during the growth reduces the oxidized nanosheets, forming the micro-porous rGO.

Fig. 2(a) and (b) shows Raman and FTIR spectra of graphenated CNTs, respectively. The most intense Raman features are the G peak at 1577 cm^{-1} and a band at around 2700 cm^{-1}, known as G′. The G band assigned to one of two modes of E_{2g} stretching vibrations corresponds to the basal plane (sp^2 domains) of single-crystal graphite or graphene [25]. The G′ band is derived from the second-order harmonic of the G band. It is known that thinner and more intense G and G′ bands are indicative of greater crystallinity of carbon-based materials [25]. The D-band (1351 cm^{-1}), on the other hand, is associated with the large amount of graphene edges and imperfection of the sigma and pi bonds formation of carbon crystals [26]; it is also relatively intense. As shown before, these imperfections allow C—O and C═O bond, which are fundamentals for HAp nuclei [22].

Fig. 2(b) shows the FTIR spectrum of rGO. The presence of carboxyl –C═O and –C–O (υ = 1741 and 1398 cm^{-1}, respectively), aromatic –C═C (υ = 1623 cm^{-1}), C—O (υ = 1288 cm^{-1}), and alkoxy –C–O (υ = 1076 cm^{-1}) bonds indicate the existence of oxygen-containing functional groups on the sample's surface [27,28]. In addition, bands localized in the range of 2910–2990 cm^{-1} are indicative of C—H methyl groups [29]. This confirms the findings from the SEM micrographs that revealed oxygen on the substrate and identifies the chemical groups that exist on the surface. It has been shown before that functional groups such as hydroxyl and carboxyl, which exist naturally as side chains of collagen molecules in the body, enhance HAp growth in a process of chemical precipitation [17,30–33]. Moreover, Zanin et al. [22] have identified carboxylic acid in particular as preferred nucleation sites for ED-HAp.

Fig. 3(a) shows the cathodic current density during the electrocrystallization of n-CaP on porous rGO at pH 3.8 and 5.8. It is evident that the current density at pH 3.8 is more negative (cathodic) than that at pH 5.8. This can be explained by addressing the main electrochemical reactions occurring on the cathode surface:

(1) $4H^+ + O_2 + 4e^- \rightarrow 2H_2O$ $\quad E^0 = 1.23$ V *vs*.SHE

(2) $H_2PO_4^- + H_2O + 2e^- \rightarrow H_2PO_3^- + 2OH^-$
$E^0 = -0.26$ V *vs*.SHE [34].

The reversible potential of each reaction (E_{rev}) is changed due to the pH of the solution and the ion concentration, as defined by the Nernst equation. However, it is evident that E_{rev} will be more negative in a higher pH solution. Therefore, it is not surprising that while applying an overpotential of −2 V, the reactions are less driven at higher pH, thus suppling less current. Fig. 3(b, c) shows that the monitored pH slightly changes during deposition. Since the solution is not buffered, this could be expected.

The initial rapid increase of cathodic current may be related to charging of the double layer in vicinity of the micro-porous rGO electrodes, when the reaction begins. The current immediately reaches steady state and remains nearly constant due to OH^- generation, which has a mass transport limitation. Moreover, the extensive hydrogen evolution at lower pH may be responsible for the noisy and unsteady current transient seen at pH 3.8. The shape of the current transient and the measured current density is somewhat different than those reported by Eliaz and Sridhar [34] for electrodeposition of HAp on CP–Ti at either pH 4.2 or pH 6.0. However, the applied potential was −1.4 V *vs.* SCE

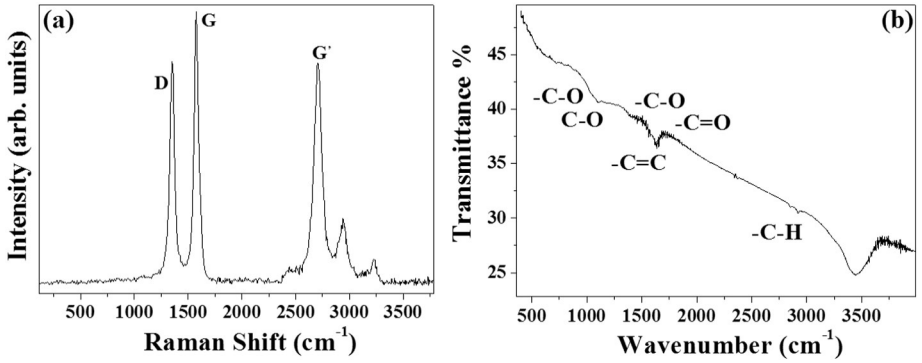

Fig. 2. (a) Raman and (b) FTIR spectra collected from as-grown micro-porous rGO samples.

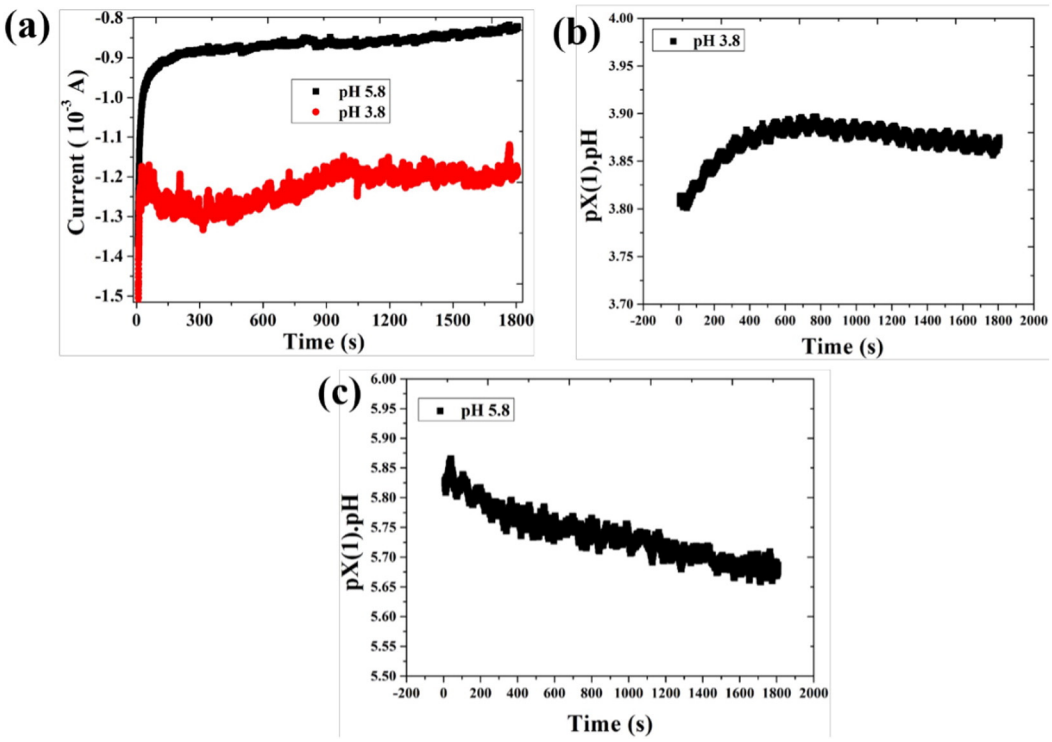

Fig. 3. Plots of (a) current density at two different pH values, (b) and (c) variation of pH over time during electrodeposition of n-CaP on micro-porous rGO electrode at pH = 3.8 and pH = 5.8, respectively.

(*i.e.* −1.356 V *vs.* Ag/AgCl), which resulted in less hydrogen evolution. In addition, both the substrate material and the electrodeposited CaP phases were different, as will be shown below.

As shown in Fig. 4, the OH^- generation is the most important control parameter for n-CaP crystal formation, because the acid-base reactions form $H_xPO_4^{-3+x}$ to PO_4^{3-}, which leads to CaP precipitation [34]. The phosphorous ions, in turn, bond to the calcium ions present at the surface by chemical attraction of the carboxylic acid, and precipitate as n-CaP [22].

Fig. 5 shows the results of the PHREEQC calculations [6,34]. In this figure, SI = 0 means that the solution is in equilibrium, SI < 0 indicates undersaturation (*i.e.*, mineral should dissolve), and SI > 0 indicates supersaturation (*i.e.*, mineral should precipitate spontaneously). From Fig. 5 we learn that monetite (DCPA) and brushite (DCPD) are not expected to form between pH 3 and pH 12. HAp may form at pH 5.8 (SI > 0 for pH > 5.0), but not at pH 3.8. Furthermore, from pH 3 to pH 12, the solution is more supersaturated with respect to TCP (and OCP) than with respect to HAp. Therefore, TCP is more likely to form, from thermodynamic consideration *per se*. As will be shown below, XRD analyses of the coatings are in line with this prediction.

Fig. 6 shows the surface morphology of n-CaP electrodeposited on porous rGO at different pH values. It can be seen that the different pH values result in a similar morphology of needle-like n-CaP, which is characteristic of nano β-TCP. The micrographs illustrate that the n-CaP crystals are uniformly distributed on the porous rGO surface. A slight difference between the two substrates is seen, more spaced crystals being grown at pH 3.8. The porosity could be explained by hydrogen bubble formation during the electrodeposition process. The surface morphology of the n-CaP coating reported herein is different from the surface morphologies of electrodeposited CaP coatings reported before by Eliaz et al. [6–8,22,29,34–42]. This may be attributed to the different substrates, electrochemical cell configuration, bath composition and pH, and applied potential. Consequently, the CaP phases that form are also different.

The average Ca/P ratio determined from the analysis was 1.5 ± 0.1 for pH 3.8 and 1.7 ± 0.2 for pH 5.8. These values should be compared to the theoretical values of atomic ratios Ca/P = 1.5 for TCP, Ca/P = 1.67 for the stoichiometric HAp [43]. It should also be born in mind that EDS is only a semi-quantitative technique; a more accurate technique such as inductively coupled plasma/mass spectroscopy (ICP-MS) or atomic absorption spectroscopy (AAS) is required for FDA approval.

As shown previously, while applying −2 V to the electrode, the pH increases near the surface of the porous rGO cathode and promotes direct n-CaP deposition on its surface. In this case, the electrostatic attraction of OH^- triggers the precipitation of n-CaP in solution.

Fig. 7 shows the XRD patterns of n-CaP crystals deposited at either pH 3.8 or pH 5.8 on porous rGO films. It should be noted that in

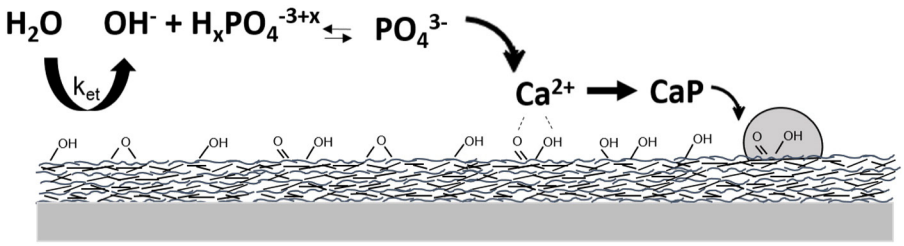

Fig. 4. The deposition mechanism of CaP on titanium covered with micro-porous rGO. k_{et} is the rate reaction constant of water reduction.

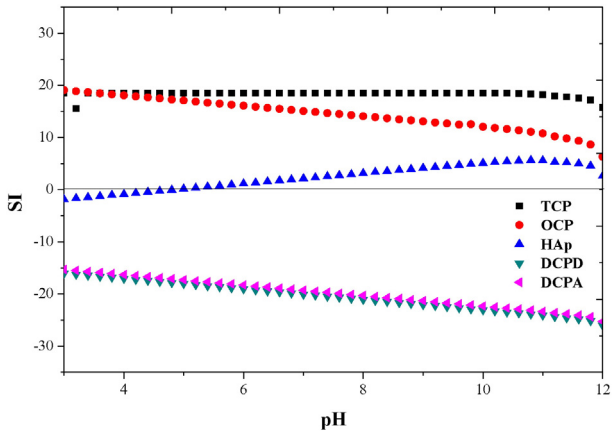

Fig. 5. Thermodynamic calculations of the saturation indices (SIs) of various CaP phases as a function of pH, for the bath composition and temperature used in this study.

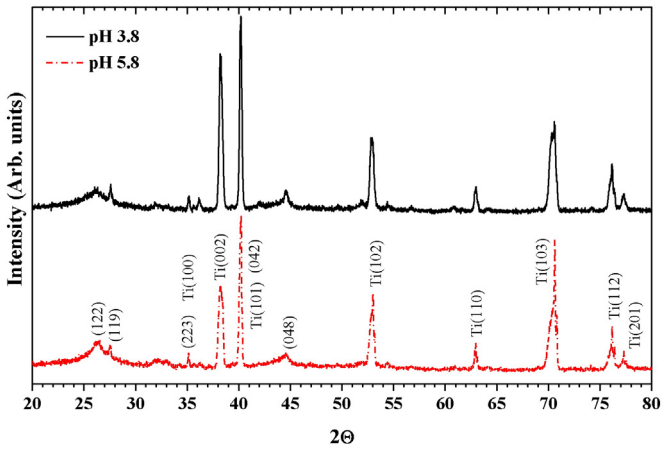

Fig. 7. XRD patterns of n-CaP deposited at two pH values. Indexing is done with respect to JCPDS 09-0169 (β-TCP powder) and JCPDS 44-1294 (titanium).

electrodeposited systems such as this one, indexing may be possible even for fairly large shifts from the card values (say interplanar spacing $d > \pm 0.01$ Å, $\Delta_{2\theta} > 0.03°$). Based on comparison to the JCPDS cards of different CaP phases it is concluded that the coating is composed of hexagonal β-TCP (JCPDS 09-0169). No evidence for HAp is found in the XRD spectra. It should be noted that no XRD reflections were observed within the range of $2\theta = 5–20°$. Baradaran et al. [11] associated a broad peak centered around 9.85° to GO, and even broader peaks centered around 24.72° and 43.54° to rGO. While we do not observe such peaks in our XRD patterns, we cannot exclude that the reflections at 26.41° and 44.56° are related to nano-crystalline (or amorphous) rGO. Porous β-TCP is a resorbable phase, regarded as an ideal bone substitute, although its use is somewhat limited by uncontrolled slow degradation rate. Nano-β-TCP can serve as a drug eluting system, *e.g.* for antibiotics. Combined with its osteoconductive properties and ability to deliver proteins and growth factors, such coatings may stimulate bone growth, reduce the risk of infection, and increase the lifetime of the implant.

Fig. 8 shows rGO/n-CaP composite samples coated at (1) pH 3.8, and (2) pH 5.8 after biomineralization assay. The samples were immersed in SBF up to 21 days and then examined using SEM and XRD. Clearly, rGO/n-β-TCP composites have high bioactivity. Growth of a uniform layer on the surface of the biomineralized samples was observed, independently of the pH during electrodeposition, with heterogeneous distribution of globular crystal agglomerations on the surface. The surface morphology is much different than that in Fig. 6(c, d). A longer incubation time of the rGO/n-β-TCP composites in SBF solution showed a similar globular

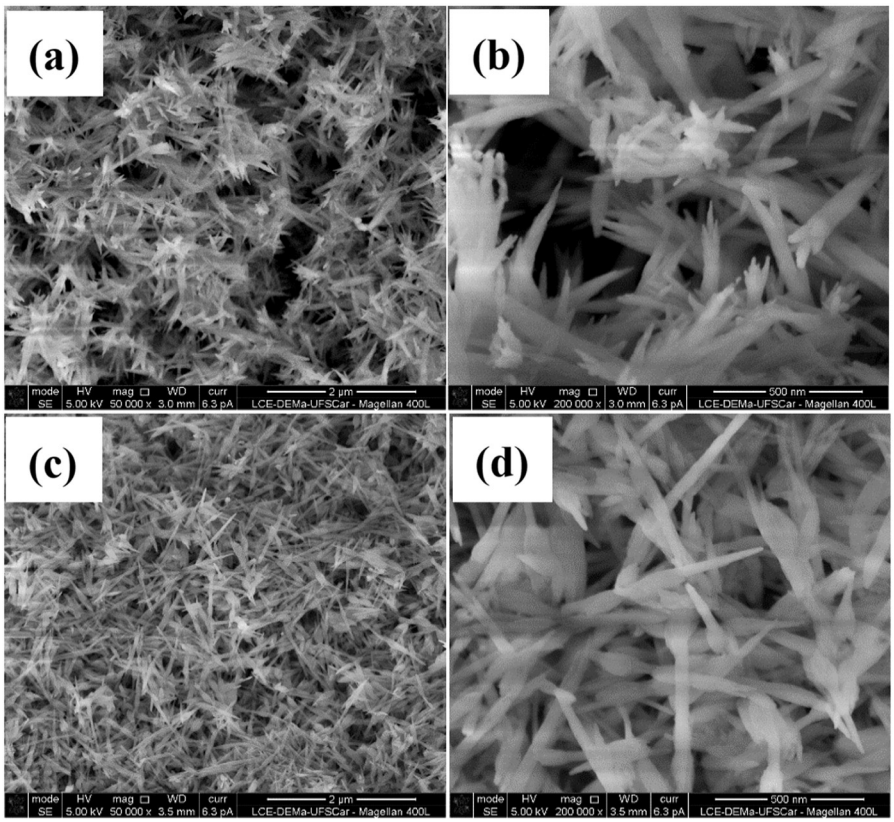

Fig. 6. SEM micrographs showing the needle-like shape of n-CaP crystals formed at pH 3.8 (a, b) and pH 5.8 (c, d).

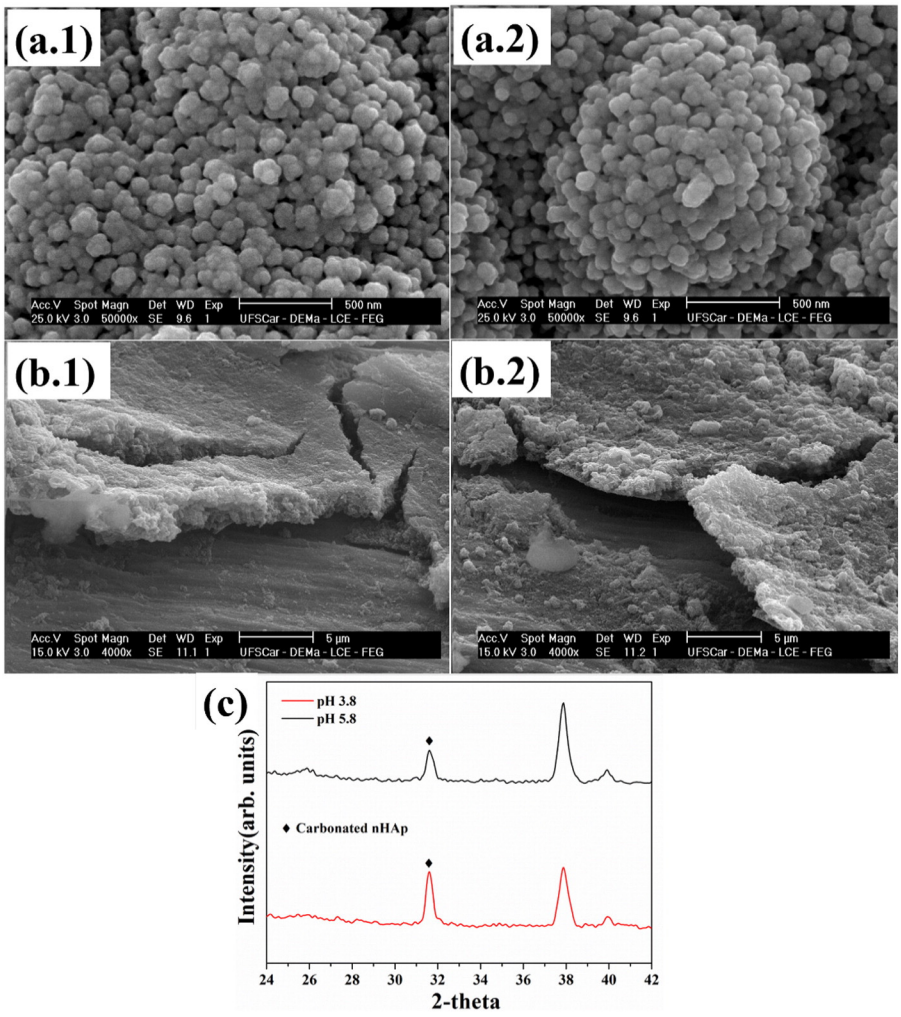

Fig. 8. Micrographs of the rGO/n-β-TCP produced at (1) pH 3.8, and (2) pH 5.8 after soaking in SBF for (a) 14, and (b) 21 days. (c) XRD pattern of rGO/n-β-TCP after soaking for 21 days in SBF solution at pH 3.8 and pH 5.8.

morphology to that discovered after 14 days (Fig. 8 (a1) and (a2)) and 21 days (Fig. 8 (b1) and (b2)). A thicker and denser layer was observed, see Fig. 8 (a2) and (b2). Moreover, the XRD pattern of the biomineralized coating was found to consist of carbonated HAp for both pH values. Fig. 8(c) shows the (211) peaks at $2\theta \approx 32°$, which is typical of carbonated HAp [44]. Calcium is one of the main elements present both in the SBF and in bioactive materials; it has an important role in the process of dissolution/precipitation. The release of this ion is one of the main factors responsible for the formation of biologically active layer and stimulus for bone growth [45]. This process of Ca ions dissolution is considered one of the determining factors in the interaction of bone with biomaterials based on CaP during cell adhesion, protein adsorption, and osteogenesis, as can be seen here. This suggests that the biomineralization process can be successfully induced, thus validating the bioactivity of the composite material.

4. Conclusions

The prime novelty of this study is both the electrodeposition of crystalline β-TCP at two different pH values and evaluation of its bioactivity. This method produces needle-like crystal with Ca/P ratio close to that of the bone. Furthermore, this new nano-biocomposite exhibits good bioactivity properties. Hence, the method of formation of n-β-TCP could be effective when used to produce bioactive nanomaterials in order to improve mechanical properties. Mechanical testing and *in vivo* assays are under examination in our group and will be presented in future publication.

Acknowledgements

The authors thank São Paulo Research Foundation (FAPESP grant: 2011/17877-7, 2011/20345-7 and 2013/09684-0), National Council for Scientific and Technological Development (CNPq grant: 474090/2013-2), Brazilian Innovation Agency (FINEP grant: 011304280) and Coordination for the Improvement of Higher Education Personnel (CAPES grant: 88887.095044/2015-00) for financial support.

References

[1] W. Suchanek, M. Yoshimura, Processing and properties of hydroxyapatite-based biomaterials for use as hard tissue replacement implants, J. Mater. Res. 13 (1998) 94–117.
[2] K.J.L. Burg, S. Porter, J.F. Kellam, Biomaterial developments for bone tissue engineering, Biomaterials 21 (2000) 2347–2359.
[3] X. Kang, W. Zhang, C. Yang, Mechanical properties study of micro- and nano-hydroxyapatite reinforced ultrahigh molecular weight polyethylene composites, J. Appl. Polym. Sci. 133 (2016), http://dx.doi.org/10.1002/app.42869.
[4] K. Zhou, X.L. Zhang, Z.C. Chen, L. Shi, W.C. Li, Preparation and characterization of hydroxyapatite-sodium alginate scaffolds by extrusion freeforming, Ceram. Int. 41 (2015) 14029–14034.

[5] W. Yu, X.X. Wang, J.L. Zhao, Q.G. Tang, M.L. Wang, X.W. Ning, Preparation and mechanical properties of reinforced hydroxyapatite bone cement with nano-ZrO_2, Ceram. Int. 41 (2015) 10600–10606.
[6] N. Metoki, L. Leifenberg-Kuznits, W. Kopelovich, L. Burstein, M. Gozin, N. Eliaz, Hydroxyapatite coatings electrodeposited at near-physiological conditions, Mater. Lett. 119 (2014) 24–27.
[7] D. Lakstein, W. Kopelovitch, Z. Barkay, M. Bahaa, D. Hendel, N. Eliaz, Enhanced osseointegration of grit-blasted, NaOH-treated and electrochemically hydroxyapatite-coated Ti–6Al–4 V implants in rabbits, Acta Biomater. 5 (2009) 2258–2269.
[8] N. Eliaz, Electrocrystallization of calcium phosphates, Isr. J. Chem. 48 (2008) 159–168.
[9] X. Zhang, Y. Zhang, X. Zhang, Y. Wang, J. Wang, M. Lu, H. Li, Mechanical properties and cytocompatibility of carbon fibre reinforced nano-hydroxyapatite/polyamide66 ternary biocomposite, J. Mech. Behav. Biomed. Mater. 42 (2015) 267–273.
[10] S. Mukherjee, B. Kundu, S. Sen, A. Chanda, Improved properties of hydroxyapatite–carbon nanotube biocomposite: mechanical, in vitro bioactivity and biological studies, Ceram. Int. 40 (2014) 5635–5643.
[11] S. Baradaran, E. Moghaddam, W.J. Basirun, M. Mehrali, M. Sookhakian, M. Hamdi, M.R.N. Moghaddam, Y. Alias, Mechanical properties and biomedical applications of a nanotube hydroxyapatite-reduced graphene oxide composite, Carbon 69 (2014) 32–45.
[12] M. Nair, D. Nancy, A.G. Krishnan, G.S. Anjursee, S. Vadukumpully, S.V. Nair, Graphene oxide nanoflakes incorporated gelatin–hydroxyapatite scaffolds enhance osteogenic differentiation of human mesenchymal stem cells, Nanotechnology 26 (2015) 161001.
[13] G. Xiong, H. Luo, G. Zuo, K. Ren, Y. Wan, Novel porous graphene oxide and hydroxyapatite nanosheets-reinforced sodium alginate hybrid nanocomposites for medical applications, Mater. Charact. 107 (2015) 419–425.
[14] J.H. Lee, Y.C. Shin, O.S. Jin, S.H. Kang, Y.-S. Hwang, J.-C. Park, S.W. Hong, D.-W. Han, Reduced graphene oxide-coated hydroxyapatite composites stimulate spontaneous osteogenic differentiation of human mesenchymal stem cells, Nanoscale 7 (2015) 11642–11651.
[15] M. Li, Q. Liu, Z. Jia, X. Xu, Y. Shi, Y. Cheng, Y. Zheng, T. Xi, S. Wei, Electrophoretic deposition and electrochemical behavior of novel graphene oxide-hyaluronic acid-hydroxyapatite nanocomposite coatings, Appl. Surf. Sci. 284 (2013) 804–810.
[16] M. Li, Q. Liu, Z. Jia, X. Xu, Y. Cheng, Y. Zheng, T. Xi, S. Wei, Graphene oxide/hydroxyapatite composite coatings fabricated by electrophoretic nanotechnology for biological applications, Carbon 67 (2014) 185–197.
[17] C. Santos, C. Piedade, P.J. Uggowitzer, M.F. Montemor, M.J. Carmezim, Parallel nano-assembling of a multifunctional GO/HapNP coating on ultrahigh-purity magnesium for biodegradable implants, Appl. Surf. Sci. 345 (2015) 387–393.
[18] A.O. Lobo, M.A.F. Corat, S.C. Ramos, J.T. Matsushima, A.E.C. Granato, C. Pacheco-Soares, E.J. Corat, Fast preparation of hydroxyapatite/superhydrophilic vertically aligned multiwalled carbon nanotube composites for bioactive application, Langmuir 26 (2010) 18308–18314.
[19] L.L. Zhang, H.J. Li, K.Z. Li, Q. Song, Q.G. Fu, Y.L. Zhang, S.J. Liu, Electrodeposition of carbonate-containing hydroxyapatite on carbon nanotubes/carbon fibers hybrid materials for tissue engineering application, Ceram. Int. 41 (2015) 4930–4935.
[20] I.A.W.B. Siqueira, M.A.F. Corat, B.D. Cavalcanti, W.A.R. Neto, A.A. Martin, R.E.S. Bretas, F.R. Marciano, A.O. Lobo, In vitro and in vivo studies of novel Poly(D,L-lactic acid), superhydrophilic carbon nanotubes, and nanohydroxyapatite scaffolds for bone regeneration, ACS Appl. Mater. Interfaces 7 (2015) 9385–9398.
[21] A.O. Lobo, I.A.W.B. Siqueira, M.F. das Neves, F.R. Marciano, E.J. Corat, M.A.F. Corat, In vitro and in vivo studies of a novel nanohydroxyapatite/superhydrophilic vertically aligned carbon nanotube nanocomposites, J. Mater. Sci. Mater Med. 24 (2013) 1723–1732.
[22] H. Zanin, C.M.R. Rosa, N. Eliaz, P.W. May, F.R. Marciano, A.O. Lobo, Assisted deposition of nano-hydroxyapatite onto exfoliated carbon nanotube oxide scaffolds, Nanoscale 7 (2015) 10218–10232.
[23] I.A.W.B. Siqueira, C.A.G.S. Oliveira, H. Zanin, M.A.V.M. Grinet, A.E.C. Granato, M.A. Porcionatto, F.R. Marciano, A.O. Lobo, Bioactivity behaviour of nano-hydroxyapatite/freestanding aligned carbon nanotube oxide composite, J. Mater. Sci. Mater. Med. 26 (2015) 113.
[24] H. Zanin, H.J. Ceragioli, A.C. Peterlevitz, V. Baranauskas, F.R. Marciano, A.O. Lobo, Field emission properties of the graphenated carbon nanotube electrode, Appl. Surf. Sci. 324 (2015) 174–178.
[25] A.C. Ferrari, J. Robertson, Raman spectroscopy in carbons: from nanotubes to diamond - preface, Phil. Trans. R. Soc. A 362 (2004) 2269–2270.
[26] A.C. Ferrari, J.C. Meyer, V. Scardaci, C. Casiraghi, M. Lazzeri, F. Mauri, S. Piscanec, D. Jiang, K.S. Novoselov, S. Roth, A.K. Geim, Raman spectrum of graphene and graphene layers, Phys. Rev. Lett. 97 (2006) 187401.
[27] J.F. Shen, T. Li, Y. Long, M. Shi, N. Li, M.X. Ye, One-step solid state preparation of reduced graphene oxide, Carbon 50 (2012) 2134–2140.
[28] O.C. Compton, B. Jain, D.A. Dikin, A. Abouimrane, K. Amine, S.T. Nguyen, Chemically active reduced graphene oxide with tunable C/O ratios, ACS Nano 5 (2011) 4380–4391.
[29] N. Metoki, L. Liu, E. Beilis, N. Eliaz, D. Mandler, Preparation and characterization of alkylphosphonic acid self-assembled monolayers on titanium alloy by chemisorption and electrochemical deposition, Langmuir 30 (2014) 6791–6799.
[30] D.P. Liu, P. Majewski, B.K. O'Neill, Y. Ngothai, C.B. Colby, The optimal SAM surface functional group for producing a biomimetic HA coating on Ti, J. Biomed. Mater. Res. Part A 77A (2006) 763–772.
[31] P.J. Majewski, G. Allidi, Synthesis of hydroxyapatite on titanium coated with organic self-assembled monolayers, Mater. Sci. Eng. A 420 (2006) 13–20.
[32] M. Tanahashi, T. Matsuda, Surface functional group dependence on apatite formation on self-assembled monolayers in a simulated body fluid, J. Biomed. Mater. Res. 34 (1997) 305–315.
[33] S. Dorozhkin, Nanodimensional and nanocrystalline apatites and other calcium orthophosphates in biomedical engineering, biology and medicine, Materials 2 (2009) 1975–2045.
[34] N. Eliaz, T.M. Sridhar, Electrocrystallization of hydroxyapatite and its dependence on solution conditions, Cryst. Growth Des. 8 (2008) 3965–3977.
[35] T.M. Sridhar, N. Eliaz, U. Kamachi Mudali, Baldev Raj, Electrophoretic deposition of hydroxyapatite coatings and corrosion aspects of metallic implants, Corros. Rev. 20 (2002) 255–293.
[36] N. Eliaz, T.M. Sridhar, U. Kamachi Mudali, Baldev Raj, Electrochemical and electrophoretic deposition of hydroxyapatite for orthopaedic applications, Surf. Eng. 21 (2005) 238–242.
[37] H. Wang, N. Eliaz, Z. Xiang, H.-P. Hsu, M. Spector, L.W. Hobbs, Early bone apposition in vivo on plasma-sprayed and electrochemically deposited hydroxyapatite coatings on titanium alloy, Biomaterials 27 (2006) 4192–4203.
[38] N. Eliaz, M. Eliyahu, Electrochemical processes of nucleation and growth of hydroxyapatite on titanium supported by real-time electrochemical atomic force microscopy, J. Biomed. Mater. Res. A 80 (2007) 621–634.
[39] N. Eliaz, W. Kopelovitch, L. Burstein, E. Kobayashi, T. Hanawa, Electrochemical processes of nucleation and growth of calcium phosphate on titanium supported by real-time quartz crystal microbalance measurements and X-ray photoelectron spectroscopy analysis, J. Biomed. Mater. Res. A 89 (2009) 270–280.
[40] N. Eliaz, S. Shmueli, I. Shur, D. Benayahu, D. Aronov, G. Rosenman, The effect of surface treatment on the surface texture and contact angle of electrochemically deposited hydroxyapatite coating and on its interaction with bone-forming cells, Acta Biomater. 5 (2009) 3178–3191.
[41] H. Wang, N. Eliaz, L.W. Hobbs, The nanostructure of an electrochemically deposited hydroxyapatite coating, Mater. Lett. 65 (2011) 2455–2457.
[42] N. Eliaz, O. Ritman-Hertz, D. Aronov, E. Weinberg, Y. Shenhar, G. Rosenman, M. Weinreb, E. Ron, The effect of surface treatments on the adhesion of electrochemically deposited hydroxyapatite coating to titanium and on its interaction with cells and bacteria, J. Mater. Sci. Mater. Med. 22 (2011) 1741–1752.
[43] S. Kale, S. Biermann, C. Edwards, C. Tarnowski, M. Morris, M.W. Long, Three-dimensional cellular development is essential for ex vivo formation of human bone, Nat. Biotechnol. 18 (2000) 954–958.
[44] S. Liao, F. Watari, G.F. Xu, M. Ngiam, S. Ramakrishna, C.K. Chan, Morphological effects of variant carbonates in biomimetic hydroxyapatite, Mater. Lett. 61 (2007) 3624–3628.
[45] X. Chen, G.S. Lee, A. Zettl, C.R. Bertozzi, Biomimetic engineering of carbon nanotubes by using cell surface mucin mimics, Angew. Chem. Int. Ed. 43 (2004) 6111–6116.